OXFORD

ORIGINAL ARTICLE

Quantitative 3D Ultrastructure of Thalamocortical Synapses from the "Lemniscal" Ventral Posteromedial Nucleus in Mouse Barrel Cortex

Javier Rodriguez-Moreno[1], Astrid Rollenhagen[2], Jaime Arlandis[1], Andrea Santuy[3,4], Angel Merchan-Pérez[3,4,5], Javier DeFelipe[3,4,6], Joachim H.R. Lübke[2,7,8] and Francisco Clascá[1]

[1]Department of Anatomy & Neuroscience, School of Medicine, Autonoma de Madrid University, 28029 Madrid, Spain, [2]Institute of Neuroscience and Medicine INM-2, Research Centre Jülich GmbH, 52425 Jülich, Germany, [3]Laboratorio Cajal de Circuitos Corticales, Centro de Tecnología Biomédica, Universidad Politécnica de Madrid, Pozuelo de Alarcón, 28660 Madrid, Spain, [4]CIBERNED, Centro de Investigación Biomédica en Red de Enfermedades Neurodegenerativas, 28031 Madrid, Spain, [5]Departamento de Arquitectura y Tecnología de Sistemas Informáticos, Universidad Politécnica de Madrid, Boadilla del Monte, 28660 Madrid, Spain, [6]Instituto Cajal, Consejo Superior de Investigaciones Científicas, 28002 Madrid, Spain, [7]Department of Psychiatry, Psychotherapy and Psychosomatics, RWTH Aachen University, 52074 Aachen, Germany and [8]JARA-Brain Medicine, 52074 Aachen, Germany

Address correspondence to Francisco Clascá, Dept. of Anatomy & Graduate Program in Neuroscience, Autónoma de Madrid University, School of Medicine, Calle Arzobispo Morcillo 4, Madrid 28029, Spain. Email: francisco.clasca@uam.es

Joachim H.R. Lübke and Francisco Clascá share senior authorship

Abstract

Thalamocortical synapses from "lemniscal" neurons of the dorsomedial portion of the rodent ventral posteromedial nucleus (VPMdm) are able to induce with remarkable efficacy, despite their relative low numbers, the firing of primary somatosensory cortex (S1) layer 4 (L4) neurons. To which extent this high efficacy depends on structural synaptic features remains unclear. Using both serial transmission (TEM) and focused ion beam milling scanning electron microscopy (FIB/SEM), we 3D-reconstructed and quantitatively analyzed anterogradely labeled VPMdm axons in L4 of adult mouse S1. All VPMdm synapses are asymmetric. Virtually all are established by axonal boutons, 53% of which contact multiple (2–4) elements (overall synapse/bouton ratio = 1.6). Most boutons are large (mean 0.47 μm³), and contain 1–3 mitochondria. Vesicle pools and postsynaptic density (PSD) surface areas are large compared to others in rodent cortex. Most PSDs are complex. Most synapses (83%) are established on dendritic spine heads. Furthermore, 15% of the postsynaptic spines receive a second, symmetric synapse. In addition, 13% of the spine heads have a large protrusion inserted into a membrane pouch of the VPMdm bouton. The unusual combination of structural features in VPMdm synapses is likely to contribute significantly to the high efficacy, strength, and plasticity of these thalamocortical synapses.

Key words: dendritic spines, serial electron microscopy, somatosensory, synaptic vesicle pool, thalamus

Introduction

Long-range projection neurons bind distant brain networks into tightly integrated functional systems. For example, the thalamocortical (TC) neurons monosynaptically link the thalamus with the cerebral cortex, and powerfully influence cortical function. Axons from neurons in different thalamic nuclei show different divergence, laminar distributions, and synaptic efficacy (Castro-Alamancos and Connors 1997). The so-called "core-type" or "lemniscal" TC neurons (Jones 1998; Clascá et al. 2016) specialize in relaying sensory information with high efficacy and temporal and spatial acuity (Ferster et al. 1996; Gil et al. 1999; Brecht and Sakmann 2002; Bruno and Sakmann 2006; Sherman 2012).

In rodents, neurons of the anterodorsal portion of the ventral posteromedial thalamic nucleus (VPMdm) relay in an highly topographic fashion mechanoreceptive information from the whisker pad to distinct domains in layer 4 (L4) of the primary somatosensory (S1) cortex called "barrels" (Killackey 1973; Pierret et al. 2000; Oberlaender et al. 2012). VPMdm neurons display high firing rates that allow them to code signals with remarkable temporal acuity. Their glutamatergic synapses elicit large postsynaptic potentials with low failure rates in excitatory L4 spiny neurons (Gil et al. 1999; Brecht and Sakmann 2002; Bruno and Sakmann 2006; Meyer et al. 2010; Kuhlman et al. 2014; Reyes-Puerta et al. 2015).

Both synaptic structure and convergent circuit patterns may contribute to the powerful effect of VPMdm inputs. Structurally, VPMdm boutons have been reported to be comparably large and to contain mitochondria, which is consistent with the elevated local energy and/or calcium homeostasis requirements of high frequency firing (Shepherd and Harris 1998). Likewise, low transmission failure may in part result from the apparent abundance of synaptic vesicles (Kharazia and Weinberg 1994; White et al. 2004; see also Holtmaat and Svoboda 2009). In contrast, large postsynaptic potentials in L4 neurons are believed to result from the spatial and temporal convergence of multiple TC and intracortical inputs (Bruno and Sakmann 2006; Schoonover et al. 2014, but see Feldmeyer et al. 1999).

Measuring the synapses of long-range projection neurons such as those of VPMdm is technically demanding, as selective, high signal-to-noise ratio labeling must be combined with fine-scale 3D electron microscopy (EM) (TEM and FIB/SEM) and specific software tools to 3D-measure large volume samples. Hence, synapses of identified VPMdm synapses remain described in qualitative terms, or, at best, as estimates from 2D EM images (Benshalom and White 1986; Lu and Lin 1993; Kharazia and Weinberg 1994; White et al. 2004). A recent 3D study using VGluT2 immunohistochemistry to label "en masse", all thalamic and claustral synapses provides a general reference (Hur and Zaborsky 2005; Bopp et al. 2017). However, since several thalamic pathways converge in S1 L4 (reviewed in Bosman et al. 2011) together with growing evidence that synapses from different thalamic nuclei may be structurally different (Da Costa and Martin 2011; Viaene et al. 2011; Familtsev et al. 2016; Bopp et al. 2017), the 3D structure of VPMdm boutons in particular remains unresolved.

Here, we combined selective anterograde labeling, 3D EM (serial transmission EM and focused ion beam milling scanning EM) and software tools to quantitatively analyze mouse VPMdm bouton structure and synaptic connections. We demonstrate a number of pre- and postsynaptic structural features whose combined effects may underlie the remarkable efficacy of VPMdm synapses.

Materials and Methods

All experimental procedures involving live animals were carried out in the Autonoma University of Madrid, in accordance with the European Community Council Directive 2010/63/UE and approved by the University's Bioethics Committee.

Surgery and Perfusion

About 6 male C57/BL6 mice (60–65 days of age) were used. Animals were housed in pairs in 20 by 30 cm cages containing some toys, and provided chow and water ad libitum under a 12 h light/dark cycle. Anesthesia was induced with ketamine (0.075 mg/g, i.p.) and xylazine (0.02 mg/g, i.p.), and maintained with isoflurane (0.5–2% in oxygen).

Animals were placed in a Kopf Instruments (Tujunga, CA, USA) stereotaxic frame. Biotinylated 10 K dextran amine (BDA; 2.5% in saline; Molecular Probes-Invitrogen, Waltham, Massachusetts, USA), was iontophoretically microinjected (0.7–0.8 μA; 1 s on/off, 30–40 min) with a Midgard Precision Current Source (Stoelting, Wood Dale, IL, USA) under stereotaxic guidance (1.6 mm posterior, 1.6 mm lateral, and 3 mm ventral to bregma; Paxinos and Franklin 2012), using borosilicate micropipettes (WPI, Sarasota, FL, USA; outer tip diameter: 7–10 μm). Following the iontophoresis, the micropipette was removed, and the muscle and skin were sutured and disinfected. After recovery, the animals were placed in individual cages. Ibuprofen (120 mg/L) was added to the drinking water to ensure analgesia.

Animals had their set of vibrissae complete at the time of sacrifice. Following a 5-days survival, animals were overdosed with sodium pentobarbital (0.09 mg/g, i.p.) and perfused though the heart with phosphate-buffered saline (0.1 M PBS) followed by 4% paraformaldehyde and 0.1% glutaraldehyde in 0.1 M PB for 30 min. Brains were removed from the skull, and post-fixed by immersion for 1 h in the same, but fresh fixative at 4 °C.

Tissue Processing

Serial 50 μm-thick coronal sections were cut with a Leica VT 1200S vibratome (Leica Microsystems, Nussloch, Germany) and collected in 0.1 M PB in 2 parallel (1:2) series. Sections were then cryo-protected by incubation in a sucrose solution (30% in 0.1 M PB) overnight, and were then rapidly freeze-thawed 3 consecutive times in liquid nitrogen.

In the first series of sections, peroxidase activity was blocked by incubation in PB-buffered oxygen peroxide for 10 min. Sections were then incubated in an avidin-biotin-peroxidase kit (1:100; Vectastain Elite™, Vector Laboratories, Burlingame, CA, USA) in PBS. After several rinses in 0.1 M PB, the bound peroxidase was revealed using the glucose oxidase-3-3′diaminobenzidine (DAB) nickel sulfate-enhanced method (Shu et al. 1988), and the sections were serially mounted onto gelatinized glass slides, lightly counterstained with thionine, dehydrated through an ascending series of ethanol, defatted in xylene, and coverslipped with DePeX mounting medium.

Light Microscopic Analysis

These mounted and coverslipped sections were used for light microscopic analysis and cytoarchitectonic localization of the injection site in the thalamus and the anterogradely labeled axons in the cortex. Sections were imaged with a Nikon Eclipse microscope equipped with a Nikon DMX1200 camera. Axonal labeling was sharp and complete, allowing the measurement of

structures near the edge of optical resolution such as varicosities and interbouton distances. Varicosity sizes (maximal projection areas) and interbouton distances (from the center of 2 consecutives boutons) were measured on the images using the polyline and polygon tools of the NIS-Elements v3.2 imaging software (Nikon, Tokyo, Japan).

In each experiment, the location and extent of the BDA deposit was reconstructed on the serial coronal sections with the aid of the thionin counterstain. Dark-field illumination and the Franklin and Paxinos atlas were used to delineate thalamic nuclei. Out of the 12 BDA injected hemispheres, 4 showed BDA injections restricted to the vibrissal domain of VPMdm (Fig. 1A, Supplementary Fig. 1) and heavy axon labeling confined to E8-9/D8 S1 barrels in S1 (Fig. 1B,C).

Tissue Preparation for Electron Microscopy

The second series of sections followed a protocol that was identical, except for the omission of the oxygen-peroxide blocking step, and the absence of nickel sulfate in the glucose oxidase-DAB development of peroxidase.

In the 4 injection experiments that produced optimal labeling of VPMdm axons in the barrel cortex (see above), free-floating sections containing the region with the heaviest cortical labeling (Fig. 1B,D) underwent further processing for EM. In these sections, the glucose oxidase-DAB reaction was followed by incubation in 1% osmium tetroxide diluted in 0.1 M PB for 45 min. Following thorough washing in 0.1 M PB, sections were first rinsed in 50% ethanol, incubated for 40 min in 1% uranyl-acetate diluted in 70% ethanol in the dark, and dehydrated in an ascending series of ethanol to absolute ethanol. The dehydrated sections were transferred to acetonitrile, and then transferred to an epoxy resin (Durcupan™, Electron Microscopy Science, Hartfield PA, USA) overnight. Finally, sections were flat-embedded in Durcupan™ and polymerized at 60 °C for 48 h. After visual inspection, samples containing the S1 neocortex were glued onto pre-polymerized resin blocks for serial TEM and imaging,

Tissue Processing for Serial TEM and Imaging

Embedded tissue blocks were then cut with a Leica Ultracut UCT ultramicrotome (Leica Microsystems, Nussloch, Germany) into serial ultrathin sections (~70–100 sections/series; ~60 nm in thickness, silver-to-gray interference contrast appearance) and collected on pioloform-coated slot copper grids. Thereafter, they were counterstained with lead citrate (3 min; Reynolds 1963), and examined with a Libra 120 transmission electron microscope (Carl Zeiss, Oberkochen, Germany). At the EM level, BDA-labeled axons were easily identifiable by the opaque DAB-reaction product. Serial digital images (20–50 per bouton) using the Multi Image Acquisition software (SIS, Olympus, Hamburg, Germany) were taken at a magnification of 8000×.

FIB/SEM 3D Tissue Preparation and Imaging

In addition, some Durcupan-embedded tissue blocks from the same experiments were glued on aluminum stubs with
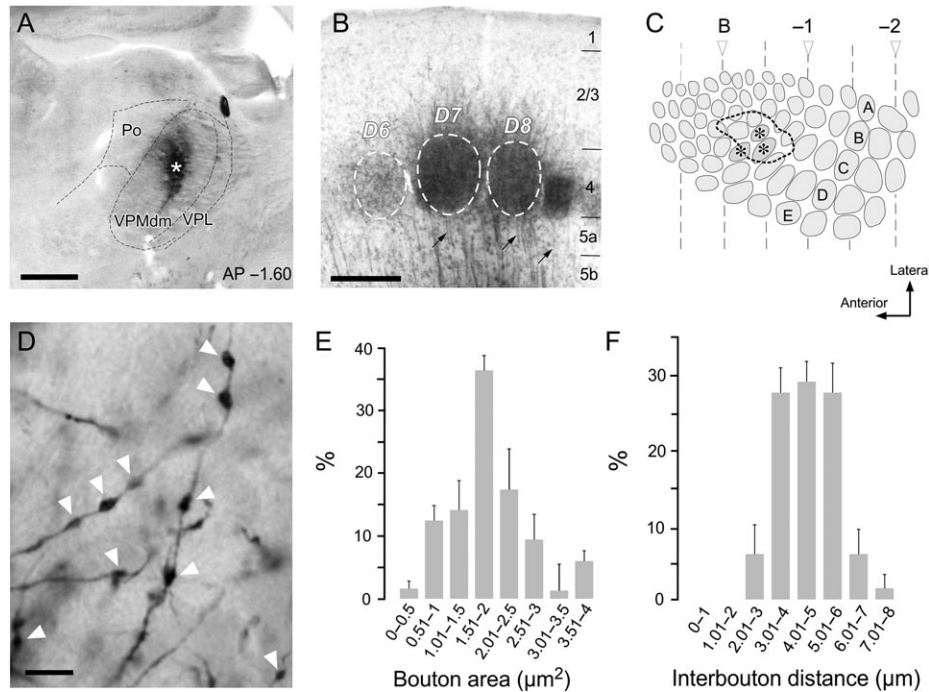

Figure 1. Selective labeling of VPMdm axons in the mouse S1 cortex. (*A*) A representative example of a stereotaxically guided iontophoretic BDA injection in VPMdm. The thionin-counterstained coronal section shows the center of the BDA microdeposit (white asterisk). Abbreviations: VPMdm, dorsomedial part of the ventral posteromedial thalamic nucleus; VPL, ventral posterolateral thalamic nucleus; Po, Posterior thalamic nucleus. Coronal level caudal to Bregma (AP; in mm) is indicated on the lower right corner (dorsal to the top, lateral to the right). (*B*) BDA-labeled VPMdm axons arborizing profusely in barrels (D6–D8 as indicated by the dashed circles) in S1. Non-branched ascending axon segments in layer 5 are indicated by black arrows. (C) Flat map reconstruction from the serial coronal sections of the barrel field zone covered by the BDA-labeled VPMdm axons in this experiment (dashed line). Anteroposterior coronal levels ("B" Bregma, −1 mm, −2 mm) are indicated on top of the map. A standard stereotaxically adjusted map of mouse L4 barrel domains (gray shaded areas) is included, for reference. Samples were taken from barrels D7–8 and E7 (asterisks). (*D*) High-magnification view of labeled axons at the core of a barrel. Note the frequent axonal varicosities of various sizes, marked by arrowheads. (*E*) Bar histogram showing the distribution in size of light microscopically identified varicosities/boutons. (*F*) Bar histogram of the distribution of intervaricosity/bouton distance. Scale bars A,B = 250 μm; D = 5 μm.

conductive carbon stickers. To avoid charge build-up artifacts, the block sides and the stub were covered with silver paint, and the block face was sputter-coated with gold-palladium.

Three-dimensional tissue samples were obtained using combined focused gallium ion beam milling and scanning electron microscopy (FIB/SEM). We used a Crossbeam 540 microscope equipped with a focused gallium ion beam and a high-resolution field emission SEM column (Carl Zeiss NTS GmbH, Oberkochen, Germany). In order to accurately identify the regions of interest, a secondary electron image was acquired from the block surface that was overlaid and collated with previously obtained light microscopy images (Merchán-Pérez et al. 2009; Bosch et al. 2015; Fig. 2A–D). Once the appropriate location was chosen, a coarse trench was milled using a 7 nA gallium ion beam to allow visualization of brain tissue under the block face. The recently milled surface was then explored and imaged

using a back-scattered electron detector (1.7–1.8 kV acceleration voltage). Automated alternate milling and imaging cycles followed, providing a stack of serial images to be reconstructed later in 3D (Fig. 2E). Fine milling cycles were performed with a 700 pA gallium ion beam, adjusted to mill a thickness of 25 nm per cycle. Imaging cycles were performed with the back-scattered electron detector at a resolution of 5 nm per pixel, so the voxel size of the resulting image stack was $5 \times 5 \times 25$ nm. About 9 stacks were obtained with a frame size of 2048×1536 pixels (field of view of 10.24×7.68 microns). The number of serial sections per stack ranged from 149 to 337; the total number of serial sections was 2050, corresponding to a total imaged volume of $4030.46 \, \mu m^3$. Registration (alignment) of serial sections was performed with Fiji software (Schindelin et al. 2012), using a rigid body model that allowed no deformation of individual images.
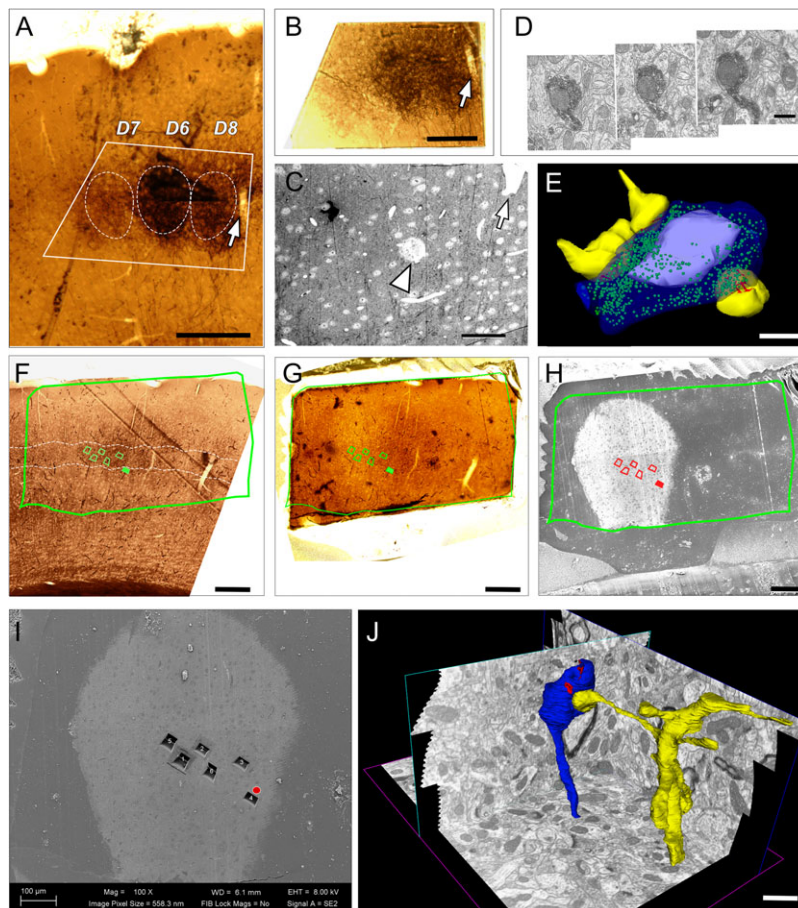

Figure 2. 3D serial TEM and FIB/SEM of identified VPMdm boutons in L4 of the S1BF. (A) Durcupan embedded 50μm-thick section containing BDA-labeled VPMdm axons in barrels D6–D8 of S1BF. This section is adjacent to that shown in Figure 1B. The trapezoid contour indicates the borders of a sample excised for subsequent serial ultrathin sectioning and TEM imaging. (B) Sample containing BDA-labeled axons, after block-mounting and trimming. Note the large blood vessel in A and B (arrow) which was used as a landmark. (C) Low power electron micrograph of an individual ultrathin section. For reference, an arrow indicates the same blood vessel in panels A–C. The bleached circle (arrowhead) is the region illustrated in D. (D) Three aligned electron micrographs from consecutive ultrathin sections showing a labeled VPMdm bouton. (E) 3D reconstruction of a VPMdm synaptic bouton (blue) shown in D establishing synaptic contact with 3 different postsynaptic spines (yellow). Note the large mitochondrion (pale blue) associated with the pool of synaptic vesicles (green). One of the PSDs (red) is also visible. (F, G) Durcupan embedded 50μm-thick section containing BDA-labeled VPMdm axons in barrels D8–D7 of S1BF. This tissue section is adjacent to that shown in Supplementary Figure 1D. The green frame indicates the borders of a sample (panel G) excised for subsequent FIB/SEM imaging. The band between the 2 white dashed lines shows the approximate borders of layer 4. (H) Secondary electron image obtained with scanning EM from the block face shown in G. (I) Secondary electron image showing several trenches milled with the focused ion beam to allow SEM imaging of brain tissue under the block face. Stacks of serial images were acquired from all trenches except the one indicated with a red dot. For precise localization, the shape of these trenches is overlaid on the images in panels F–H. (J) 3D FIB/SEM reconstruction of a labeled axonal segment giving rise to a synaptic bouton (blue) with 2 PSDs (red) on a 3-axis background view of the neuropil. A spine postsynaptic to the bouton and its parent dendrite (yellow) is also 3D-reconstructed. Scale bars: A, F–H = 250 μm; C = 5 μm; D, J = 0.5 μm; E = 0.25 μm; I = 100 μm.

3D Reconstruction and Analysis

Digital 3D volume reconstructions and measurements of serial TEM images was carried out with the OpenCAR software (Contour Alignment Reconstruction; Sätzler et al. 2002). Digital images were aligned creating an image stack where all structures of interest were defined by closed contour lines of different color. We made area measurements both of the PSD object contour and of the synaptic interface (apposition) area. These 2 parameters are different: the PSD object contour is a measurement of the surface of the 3D closed envelope around the whole electron-dense structure opposing the synaptic cleft, whereas the synaptic interface area is the surface obtained by measuring its length on each section and multiplying by section thickness and the number of sections traversed. Thus, PSD contour area is roughly the double of the synaptic interface area. Both measurements have been used by different authors (PSD object contour: Rollenhagen et al. 2015; Dufour et al. 2016; or interface area: Arellano et al. 2007; Bopp et al. 2017; Hsu et al. 2017). Here, we provide both parameters to make comparisons straightforward.

The Z-stack image series acquired with FIB/SEM were 3D-segmented and measured with Espina Interactive Neuron Analyzer software (v.2.1.10; freely available at http://cajalbbp. cesvima.upm.es/espina/, Morales et al. 2011). PSD interface was measured as the area of the synaptic apposition surface, which was extracted with Espina software from the 3D reconstructions of synaptic junctions (Morales et al. 2013). The 3D reconstructions generated from separate Z-stacks were digitally stitched using Unity 3D modeling software (Unity Technologies, San Francisco CA, USA)

Only complete synaptic boutons (i.e., those which could be followed from the beginning to their end in consecutive serial sections) were included in our analysis. The geometry of VPMdm synaptic boutons, the PSD, mitochondria and the vesicle pool within individual boutons, and the postsynaptic profiles contacted by the synaptic boutons were reconstructed and quantified. From the contours, 3D volumetric reconstructions were performed, from which surface and volume measurements were obtained.

In 12 of the presynaptic VPMdm boutons imaged by TEM where the DAB-reaction product was light enough in order to define vesicles confidently, the number of synaptic vesicles was estimated. We applied the Physical Disector stereological method to avoid double counting in contiguous serial sections (Sultan et al. 2002).

For each parameter, the mean ± standard deviation (SD), the median, maximum and minimum, and coefficient of variation (CV) were calculated.

Results

Light Microscopic Visualization of VPMdm Axons in the S1 Barrel Cortex

Thalamocortical axons were labeled by anterograde transport of BDA following iontophoretic microinjections placed in VPMdm under stereotaxic guidance (Fig. 1A). Four experiments in which the BDA deposit was restricted to the "barreloid" domain of VPMdm (Fig.1A and Supplementary Fig. 1) were selected for EM analysis. Neurons in VPMdm are known to relay information from the anterior macrovibrissae to S1 in a highly topographic fashion (Land et al. 1995). Heavy axonal labeling was observed in L4 of the vibrissal region of the primary somatosensory cortex (S1BF, Figs 1B and 2A,B; Supplementary Fig. 1). Two-dimensional

reconstruction of S1BF from the aligned serial coronal section contours revealed that the most heavily labeled barrels were D7-8/E7 (Fig 1C).

A thick plexus of heavily labeled axons delineated sharply the L4 barrels (Fig. 1B,D). Labeled axons extended into L2/3, but were absent in L1. In L6a, a sparser plexus of labeled axonal arborizations was present under the area containing L4 labeling (not shown). In contrast, L5a and L5b contained only unbranched, vertically oriented axonal segments (Fig. 1B). Occasional, isolated retrogradely labeled L6 pyramidal cell somata were often observed under the labeled barrels (not shown).

High-power light microscopic examination showed that labeled L4 axons are densely covered with varicosities (putative synaptic boutons) separated by much thinner axonal segments. (Fig. 1D). These varicosities were of variable size ranging in surface area from 0.4–3.7 μm^2 (mean 1.83 ± 0.75 μm^2) with a skew towards larger synaptic boutons. Interbouton distances ranged between 2.4 and 7.3 μm (mean 4.60 ± 1.16 μm; see also Fig. 1E,F).

Serial TEM Analysis of VPMdm Boutons

The sections adjacent to those found to contain the heaviest labeling in S1BF neocortex in the light microscopic analysis were processed for EM (see Methods; Fig. 2A,B). We focused our analysis on the central zone of the D7-8/E7 barrel domains (Fig. 2A–C).

In the serial TEM analysis, a total of 64 BDA-labeled synaptic boutons from 4 different experimental animals were reconstructed. Labeled boutons were identified by the electron-dense DAB-reaction product throughout the synaptic bouton and its associated axonal segments (Fig. 2D). Bouton sampling was essentially random, as any labeled bouton that could be completely reconstructed from a given series of ultrathin sections was analyzed. Individual BDA-labeled boutons and their target structures were imaged in consecutive ultrathin sections (Fig. 2D), 3D-reconstructed and measured (Fig. 2E; Figs 5 and 6, in blue).

"En passant" boutons were more frequently found (n = 42; 65.6%) than terminal boutons (n = 22; 34.4%). Synaptic complexes, composed of a synaptic boutons and its target structure, were identified by the presence of distinct, parallel pre- and postsynaptic membranes separated by a synaptic cleft and a band of postsynaptic dense material adherent to the cytoplasmic surface of the postsynaptic membrane, and a pool of synaptic vesicles within the presynaptic bouton (Gray 1959a,b; Peters and Palay 1996). In all cases, PSDs opposed to labeled synaptic boutons were dense and thick, thus corresponding to asymmetric synapses (Colonnier 1968).

Mitochondria were clearly visible (Figs 2D, 3, 4, and 5A1–3). In the less heavily stained synaptic boutons, it was even possible to clearly identify all synaptic vesicles (Fig. 4; Figs 5A1–3 and 9, in green). However, the BDA-labeling obscured a clear delineation of the presynaptic density (Figs 3, 4, and 5A1–3).

The 64 serial TEM-reconstructed boutons (Fig. 6, in blue) established 105 synapses. The majority of synapses (83%) were established on dendritic spines of different shape and size (Table 1) including mushroom (Fig. 4), stubby and elongated ones. Synapses on dendritic shafts were less common (17%; Fig. 3A,B; Table 1). In the majority of cases (53%) individual boutons were found to establish multiple synaptic contacts with 2 or more dendritic spines (Fig. 4B,C; Table 1), or with 2 different postsynaptic elements, for example with a dendritic shaft and a dendritic spine (Fig. 3D). Occasionally, 2 or 3 labeled synaptic boutons established synapses with the same dendritic shaft at
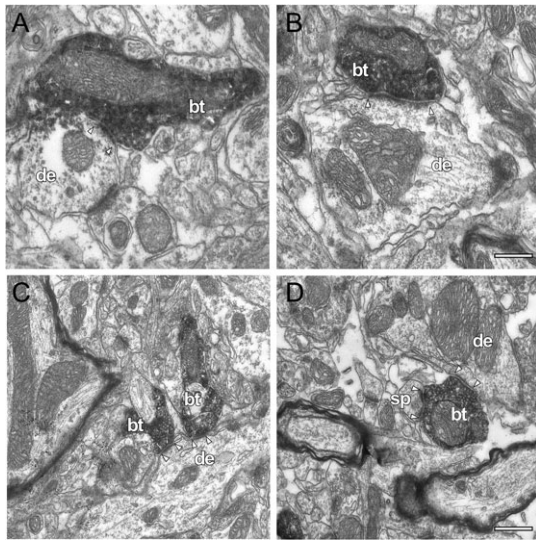
Figure 3. Serial TEM micrographs of BDA-labeled VPMdm thalamocortical boutons (bt) establishing synaptic contacts with dendritic shafts (de). (*A, B*) VPMdm synaptic boutons establishing synaptic contacts with dendritic shafts. (*C*) Two synaptic boutons terminate in close proximity on the same dendritic segment. (*D*) Individual synaptic bouton innervating both a dendritic shaft and spine (sp). Note that the PSDs (arrowheads) are of different shape and size, but always non-perforated. In all figures, PSDs are marked by arrowheads. Scale bars *A,B* = 0.25 μm; *C,D* = 0.5 μm.
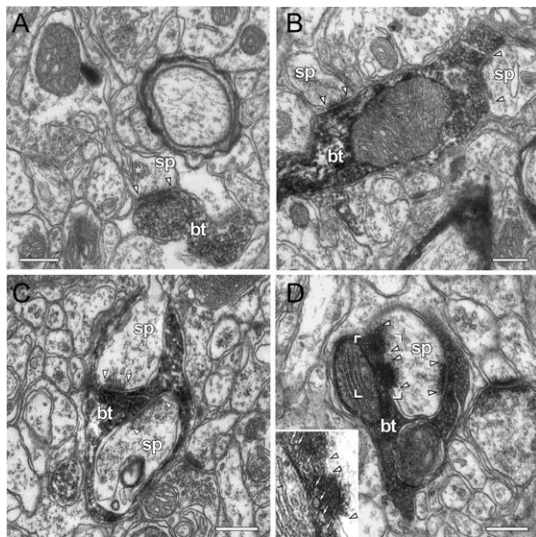

Figure 4. Serial TEM VPMdm boutons (bt) establishing synaptic contact with dendritic spines (sp). (*A*) A labeled VPMdm bouton synapsing on a dendritic spine head. A spine apparatus is indicated by an asterisk. (*B*) Two dendritic spines innervated by the same VPMdm bouton. (*C*) Two spine heads completely enwrapped by the bouton (*D*) VPMdm bouton establishing 2 synaptic contacts with the same dendritic spine (1 non-perforated and 1 perforated). Inset: higher-magnification of one of the PSDs (frame area in *D*). Some synaptic vesicles are indicated by white arrows. In all figures PSDs are marked by arrowheads. Scale bars *A–D* = 0.25 μm.

Figure 5. Serial TEM 3D-volume rendering of VPMdm boutons. (*A1–3*) Three consecutive ultrathin sections of a BDA-labeled VPMdm bouton. Large numbers of presynaptic vesicles (given in green) are distributed throughout the terminal. The PSD is highlighted in red and marked by arrowheads. (*B–F*) Examples of 3D-volume reconstructions of individual boutons. In each panel, the outline of the bouton (blue) and PSDs (red) are represented at the top. The bouton's mitochondria (white) and pool of synaptic vesicles (green) are shown at the bottom. Note the different shape and size of the PSDs. Scale bars *A–F* = 0.5 μm.

close range (Fig. 3C). The majority (~70%) of the postsynaptic dendritic spines contained a spine apparatus (Fig. 4A,B; Supplementary Fig. 2A). According to the criteria of Peters et al. (1991) we identified a spine apparatus as 2 or more membrane-bound sacs or cisternae, alternating with thin laminae of dense material. In 40% the head of the dendritic spines was partly embedded into the bouton, thus substantially increasing the
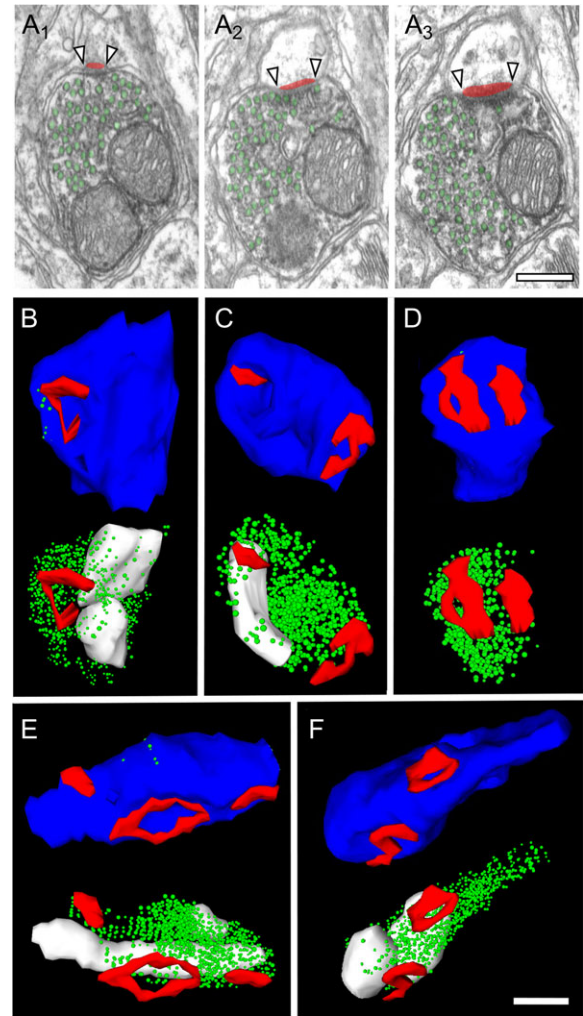
apposition area beyond the PSD zone (Fig. 4C,D). We did not find VPMdm axon varicosities lacking a synaptic specialization.

Most labeled VPMdm synaptic boutons (87.5%, Table 1) contained 1, or even several mitochondria of different shape and size (Figs 3A–D, 4B,D, and 5); they were more abundant in the largest boutons (Figs 3D and 5A,D,E, in white). Mitochondria contributed, on average, ~25% to the bouton total volume.

In twelve of the synaptic boutons of our sample, the electron-dense labeling was light enough to allow the unambiguous counting of presynaptic vesicles (Figs 4D and 5A1–3 in green, and Table 1). In these boutons, the total pool of synaptic vesicles was 3D-reconstructed and counted. Unfortunately, the DAB-reaction product made it impossible to estimate the distance of individual synaptic vesicles from the presynaptic density, which would have allowed the definition of the so-called "docked" vesicles constituting the readily releasable pool, or vesicles close to the presynaptic density, which may resemble the recycling pool and reserve pool.
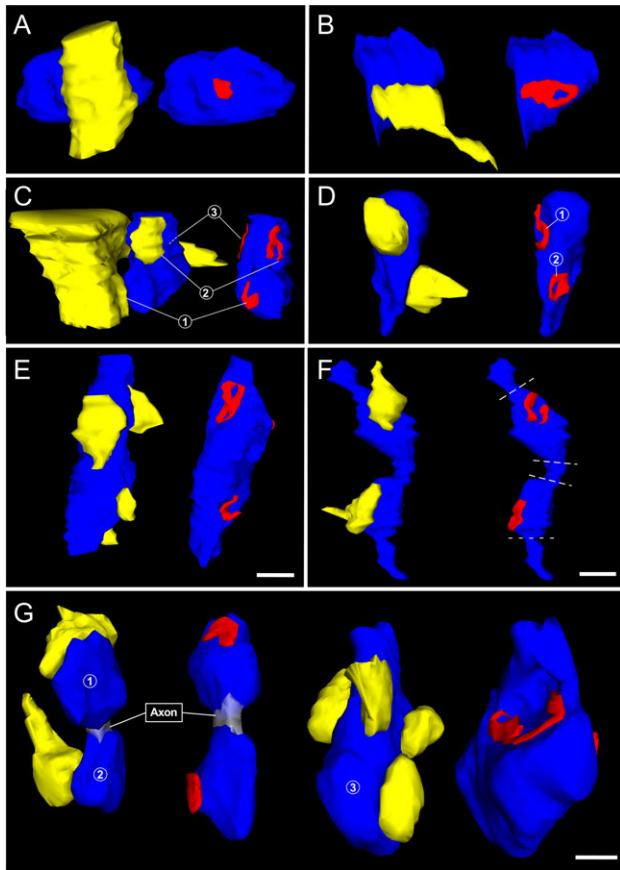
Figure 6. Serial TEM 3D-volume rendering of VPMdm boutons (blue) establishing synaptic contacts (red) onto dendritic shafts and spines (yellow). (A) A bouton with a non-perforated PSD terminating on a dendritic shaft. (B) A bouton establishing a synaptic contact with a dendritic spine with a ring-like perforation of its PSD. (C) A bouton with 3 PSDs contacting a dendritic shaft (1) and 2 separated spines (2 and 3). (D) A bouton with a horseshoe-like perforated (1) and a ring-like perforated PSD (2) terminating on 2 individual dendritic spines. (E) A bouton innervating 4 dendritic spines. Note the different shape and size of the PSDs. (F) *En passant* axon with 2 synaptic boutons contacting 2 dendritic spines (dashed line indicates the borders of the boutons). (G) Three labeled boutons (1–3) in close proximity to each other establishing 1 (1–2) and 4 (3) synaptic contacts with dendritic spines. Note the different size of the 3 boutons. All PSDs are represented in red. Scale bar A–G = 0.5 μm.

Ultrastructural Characteristics of PSDs

The PSDs from both dendritic shafts and dendritic spines post-synaptic to VPMdm boutons displayed several sizes and forms. Their mean size was large (0.1 ± 0.5 μm^2). Most displayed complex morphologies within the same postsynaptic element: horseshoe-shaped (32.2%; Figs 5*B*,*C* and 6*C*–*G*, in red), ring-like perforated (9.5%; Figs 5*E*,*F* and 6*B*,*D*,*E*, in red), or fragmented/partitioned (several irregular small disc-shape with no connection between them; 6.2%; Figs 5*D* and 6*F*, in red). The remaining PSDs (48%) were disc-shaped (Figs 5*C*,*E* and 6*A*,*F*,*G*, in red).

We analyzed 74 dendritic spines postsynaptic to VPMdm boutons using serial TEM. In most cases, only the head and adjacent parts of the neck could be reconstructed. In a small sample (*n* = 20), dendritic spines could be followed to its origin at the dendritic shaft. Boutons were seen to contact a variety of different types of dendritic spines (stubby, thin and mushroom), with a prevalence of mushroom-shaped spines (Fig. 6*C*, in yellow; Arellano et al. 2007).

FIB/SEM 3D Analysis of VPM Axons and Synapses

A total volume of 4050 μm^3 of S1 L4 neuropil was imaged using focused ion beam milling scanning EM (FIB/SEM). The resolution used (5 nm per pixel) for scanning large tissue volume samples was enough to delineate and measure with confidence axonal membranes, mitochondria, postsynaptic spines, and most PSDs. In this case, sampling was not restricted to varicose enlargements, but also intervaricose segments were serially imaged.

The scanned volume contained 15 labeled VPMdm axonal segments (one of them ramified) that presented 37 boutons along a total linear axonal length of 165 μm (Fig. 7) (average interbouton distance = 4.4 μm/bouton). The mean interbouton segment diameter was 0.30 ± 0.1 μm.

The 37 boutons established 54 synapses (1.5 synapses per bouton; mean 0.34 synapses/μm of total axon length). Although the vast majority of synapses were established by "boutons" (i.e., varicose enlargements), 3 synapses (5.3%) were located in "inter-varicose" axon segments (i.e., segments with a diameter smaller than 0.5 μm) that did not contain mitochondria. Among these, 12 boutons were sharply visualized enough to confidently measure their surface and volume, mitochondrial volume and PSD, and to pool these data with those obtained from serially sectioned TEM material (Table 1).

In the FIB/SEM-studied neuropil, 30 spines postsynaptic to the labeled VPMdm axons could be reconstructed completely (to the shaft of their parent dendrite) and measured. These spines were predominantly long and mushroom-shaped (Fig. 8). In this sample, as with serial TEM, larger PSDs were always located on large-headed dendritic spines. Some (~15%) of the dendritic spines that received a synapse from a VPMdm bouton were also targeted by an unlabeled symmetric synapse of unknown origin (Fig. 8, Table 1). As with TEM, spine apparatuses could be recognized in many of the spines postsynspatic to VPMdm boutons (Fig. 8); however, their fine structure of their cisternae was obscured by the relatively low resolution used in the SEM image acquisition (Supplementary Fig. 2). The presence of a spine apparatus was strongly associated with large spine heads (in line with previous studies, e.g., Peters et al. 1991) most of which had spine protrusions (Fig. 8).

As in the TEM sample, we observed with FIB/SEM many dendritic spine heads partially intruding into the labeled VPMdm boutons (Figs 4*C*,*D* and 9). The intruded surface always included the PSD, and created an additional zone of direct apposition between the pre- and postsynaptic membranes. Moreover, in a sizable proportion of the dendritic spines (12/92; 13% of the total reconstructed with serial TEM or FIS/SEM) a large finger-shaped protrusion was seen deeply inserted into a deep membrane pouch of the labeled VPMdm bouton. These remarkable protrusions were of about the same caliber than the rest of the head, and thus considerably increased beyond the PSD (up to 26 times) the apposition area between dendritic spine and bouton (Fig. 9*B*–*D*).

Quantitative Analysis of Various Structural Parameters of VPMdm Synaptic Boutons

The 3D-volume reconstructions based on serial TEM or FIB/SEM sections allowed the quantification of structural and subcellular elements (Table 1). Boutons varied substantially in both shape and size (Figs 5–7). Their mean surface area was 4.67 ± 2.20 μm^2 (min: 1.26 μm^2; max: 11.58 μm^2) with a mean volume of

Table 1 Quantitative analysis of structural parameters of VPMdm synaptic boutons

Boutons (n = 76)

Synapses per bouton	Synapses on spines vs. dendritic shafts	Bouton surface (μm²)		Bouton volume (μm³)
1.6	83% vs. 17%	Range	1.26 –11.58	0.06 –1.59
		Mean ± SD	4.67 ± 2.20	0.46 ± 0.27
		Median	4.42	0.42
		CV	0.47	0.59

Mitochondria (n = 68)

% of boutons containing mitochondria	% of mitochondrial volume to bouton volume	Mitochondrial volume per bouton (μm³)	
92%	23.03%	Range	0.01–0.25
		Mean ± SD	0.09 ± 0.06
		Median	0.09
		CV	0.58

Vesicle pools (n = 12)

No. of vesicles per bouton

Range	200–1095
Mean ± SD	740 ± 285
Median	795
CV	0.39

PSDs (n = 124)

PSD shape		PSD interface surface (μm²)		PSD contour area (μm²)	PSD on shafts contour area (μm²)	PSD contour area on spines (μm²)
Disc	48.6%	Range	0.01–0.24	0.03–0.47	0.08–0.46	0.03–0.47
Horseshoe	35.2%	Mean ± SD	0.1 ± 0.5	0.21 ± 0.11	0.2 ± 0.09	0.21 ± 0.11
Perforated	9.5%	Median	0.09	0.2	0.18	0.2
Fragmented	6.7%	CV	0.50	0.51	0.45	0.52

Postsynaptic spines (n = 92)

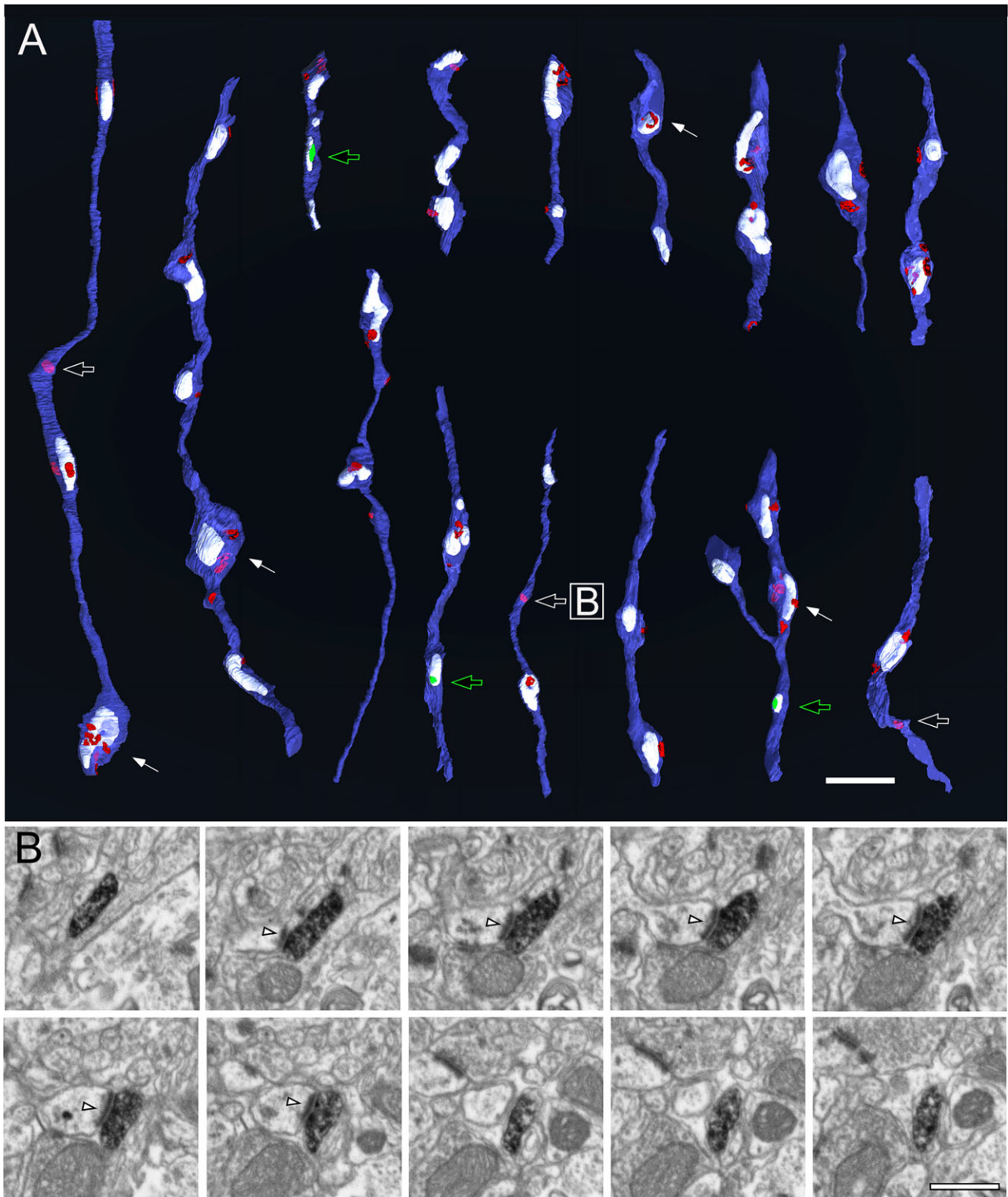| Spines with an additional (symmetric) synapse	Spine head surface (μm²)		Spine head volume (μm³)
15%	Range	0.17–1.98	0.004–0.18
	Mean ± SD	0.87 ± 0.47	0.06 ± 0.04
	Median	0.94	0.06
	CV	0.54	0.62

Figure 7. VPMdm axonal segments 3D-reconstructed from FIB/SEM image stacks. (A) 3D reconstructions of fifteen axonal segments. Axonal membrane is represented in transparent blue to visualize mitochondria (white). PSDs in spines are colored in red. PSDs in dendrite shafts are colored in green and pointed by an open green arrow. White arrows indicate the location of a protrusion into the VPM bouton from the postsynaptic spine (see Fig. 9). Open white arrows indicate PSDs located in non-varicose axon domains containing mitochondria. Note that the latter lack nearby mitochondria. (B) Samples form a series of FIB/SEM images showing the synapse marked with the letter "B" in panel A. Images shown are spaced 75 nm. The dark BDA precipitate is clearly visible within this non-varicose axonal segment. The arrowhead points to a PSD on a dendritic spine. Scale bars A = 2 μm; B = 0.5 μm.
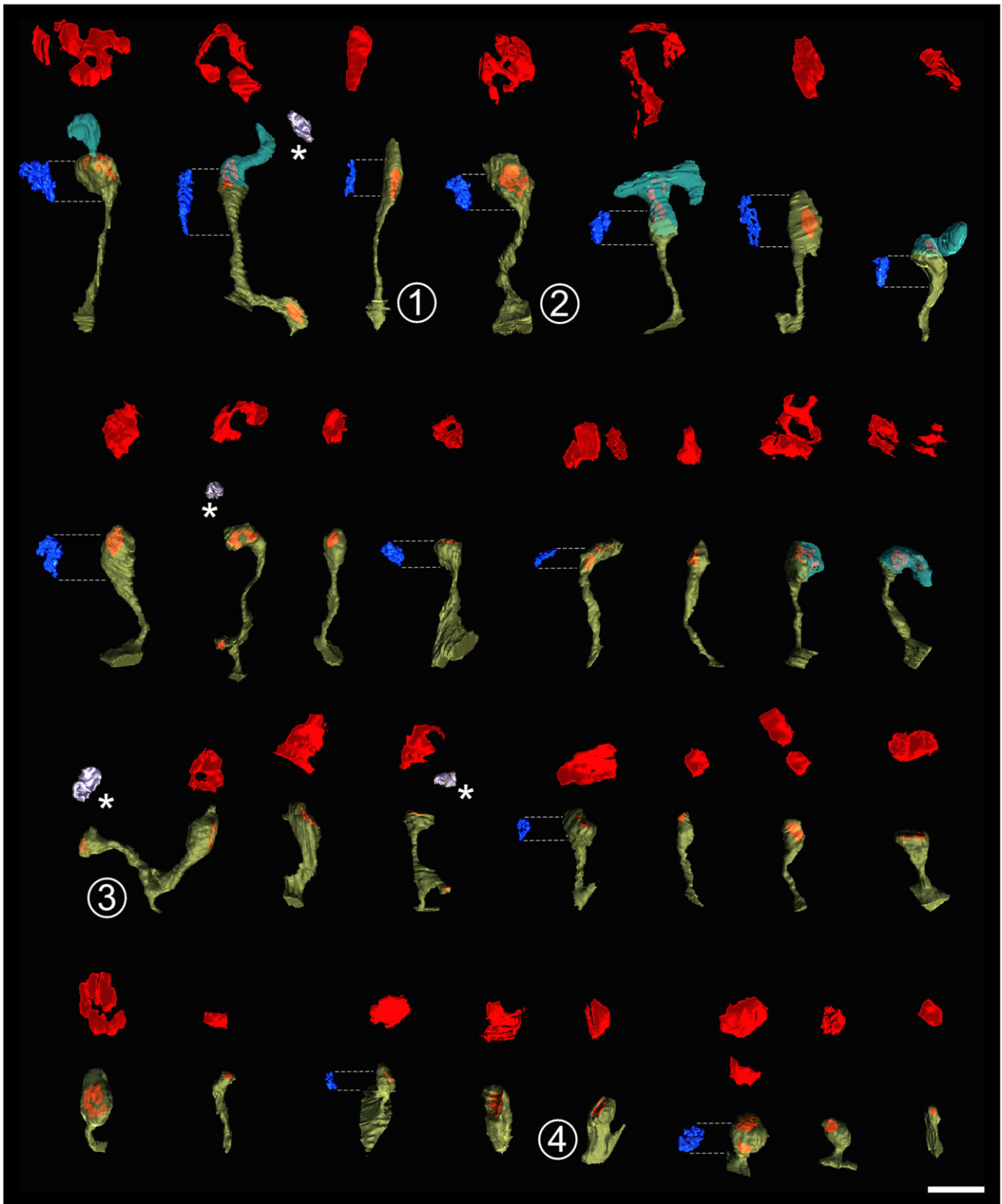
Figure 8. Spines of different shape and size postsynaptic to identified VPMdm boutons 3D-reconstructed from FIB/SEM image stacks. About 30 spines with varying shapes were reconstructed. Typical "filopodial" (1), "mushroom" (2), "branched" (3), and "stubby" (4) shapes can be observed. The spine membrane (yellow) is made transparent to allow visualization of the PSDs (red). In addition, PSDs are shown on top of each spine, rotated and at double magnification, to better visualize their shape. PSDs in gray and indicated with an asterisk are those located on the same spine but not corresponding to a contact with a labeled VPM axons. Non-synaptic zones of the spine intruded inside VPMdm boutons are indicated by a blue–green shade on some spines. In those spines with a visible spine apparatus, a 3D reconstruction of this organelle (in blue) is shown on the left of the corresponding spine. Scale bar = 0.5 μm.

$0.46 \pm 0.27 \,\mu m^3$ (min: $0.06 \,\mu m^3$; max: $1.59 \,\mu m^3$). Both values were highly correlated ($r = 0.904$; $P < 0.00001$; Fig. 10A).
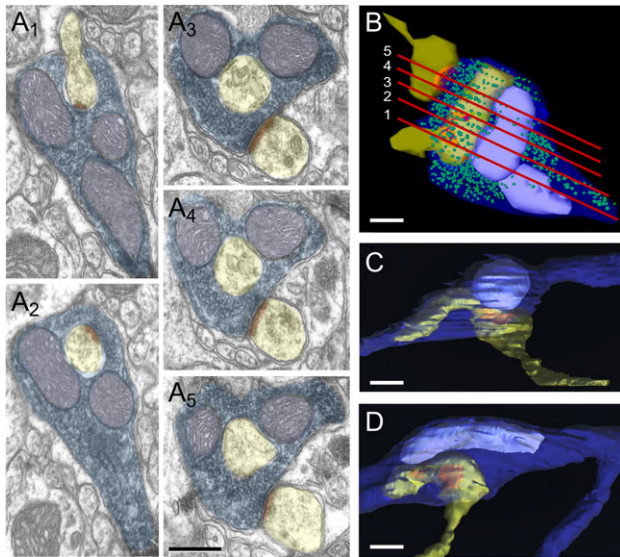

Figure 9. Spine protrusions embedded into VPMdm boutons. (A1–5) Serial TEM images of a synaptic bouton (transparent blue) containing a large spine protrusion (transparent yellow) deeply inserted into it. Mitochondria are shaded in purple, and the PSD in brown. (B) 3D reconstruction of the same synapse. Images in panels A1–5 correspond, respectively, to levels 1–5 in this reconstruction, and are colored likewise. The synaptic vesicles (green) are also shown in the 3D reconstruction. (C,D) Two additional examples of spines with large spine protrusions invading VPMdm boutons reconstructed from FIB/SEM samples. Same color code as in panel B. Scale bars = $0.25 \,\mu m$.

Bouton size measured as maximal projection area is a parameter useful for comparisons with axonal varicosities measured in studies of stained or fluorescent axons using high-magnification optical microscopy (Fig. 1; see also Viaene et al. 2011; Marion et al. 2013). The maximal projection area for our sample of both FIB/SEM and serial TEM-reconstructed boutons was $1.12 \pm 0.61 \,\mu m^2$. Interestingly, this value include was 40% smaller than that of the projection areas we measured using ×1000 oil-immersion, 1.4 N.A. objectives on avidin-biotin-peroxidase-DAB-nickel stained VPMdm axons on adjacent sections of the same experiments (Fig. 1E). Since the visualization resolution is roughly comparable with both methods, at least for the larger boutons, the difference probably reflects a down-sampling of smaller boutons in the optical analysis.

In nearly all boutons, mitochondria were present, often more than 1, and up to 4. They were distributed across the entire terminal, always closely associated with the synaptic vesicle pool (Table 1). The mean mitochondrial volume in a bouton ($0.99 \pm 0.06 \,\mu m^3$) was highly correlated with bouton volume ($r = 0.728$; $P < 0.00001$; Fig. 10B).

We performed area measurements both of the PSD contour and of the synaptic interface. PSD contour was $0.21 \pm 0.11 \,\mu m^2$ (min: $0.03 \,\mu m^2$; max: $0.47 \,\mu m^2$; Table 1) and PSD interface $0.1 \pm 0.5 \,\mu m^2$. Differences in PDS size between shaft and dendritic spine PSDs were minimal (Fig. 10D). Furthermore, a weak correlation was found between PSD surface (sum of all PSDs in a bouton) with bouton surface ($r = 0.207$; $P = 0.02$; Fig. 10C).

Correlations between PSDs and dendritic spine morphologies were also examined. The mean surface area of the dendritic spine heads is $0.87 \pm 0.47 \,\mu m^2$ (min: $0.17 \,\mu m^2$; max: $1.98 \,\mu m^2$) with a mean volume of $0.06 \pm 0.04 \,\mu m^3$ (min: $0.004 \,\mu m^3$; max: $0.18 \,\mu m^3$). The spine heads postsynaptic to the VPMdm boutons showed a wide range of sizes (Table 1,
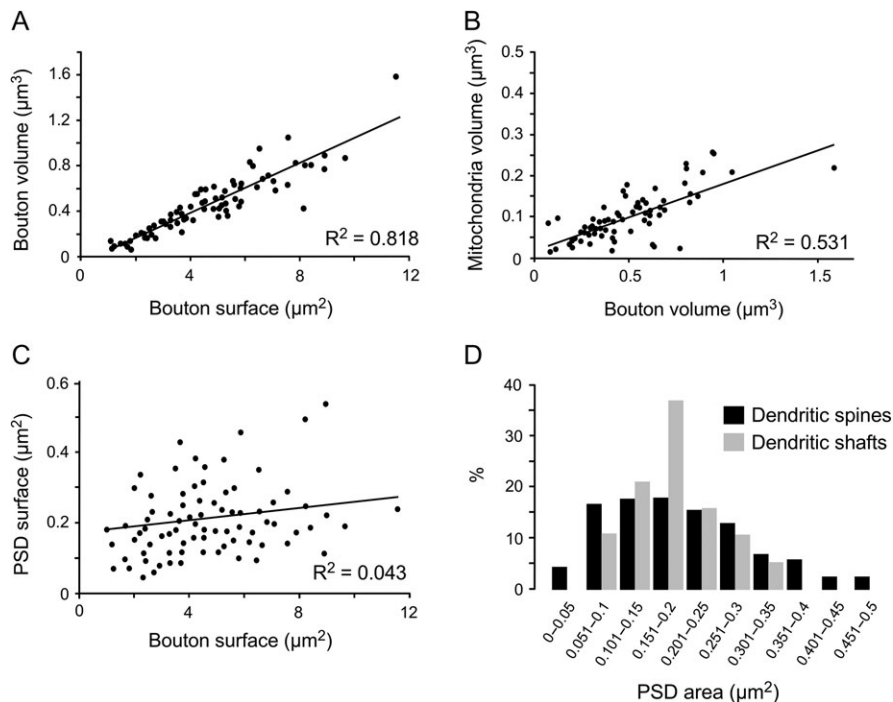

Figure 10. Correlations between different structural parameters of the VPMdm boutons (I). Serial TEM and FIB/SEM data are pooled together. (A) Dot plot correlation analysis between bouton surface vs. volume. Note the high correlation as indicated by the linear regression and R^2. (B) Between bouton volume vs. mitochondrial volume. (C) Bouton surface area vs. PSDs contour surface area. Note that both parameters are not correlated, as indicated by the R^2. (D) Bar histogram of the distribution of PSD contour surface area for dendritic spines and shafts. There were no statistically significant differences between the 2 distributions ($P = 0.876$, Kolmogorov–Smirnov test).
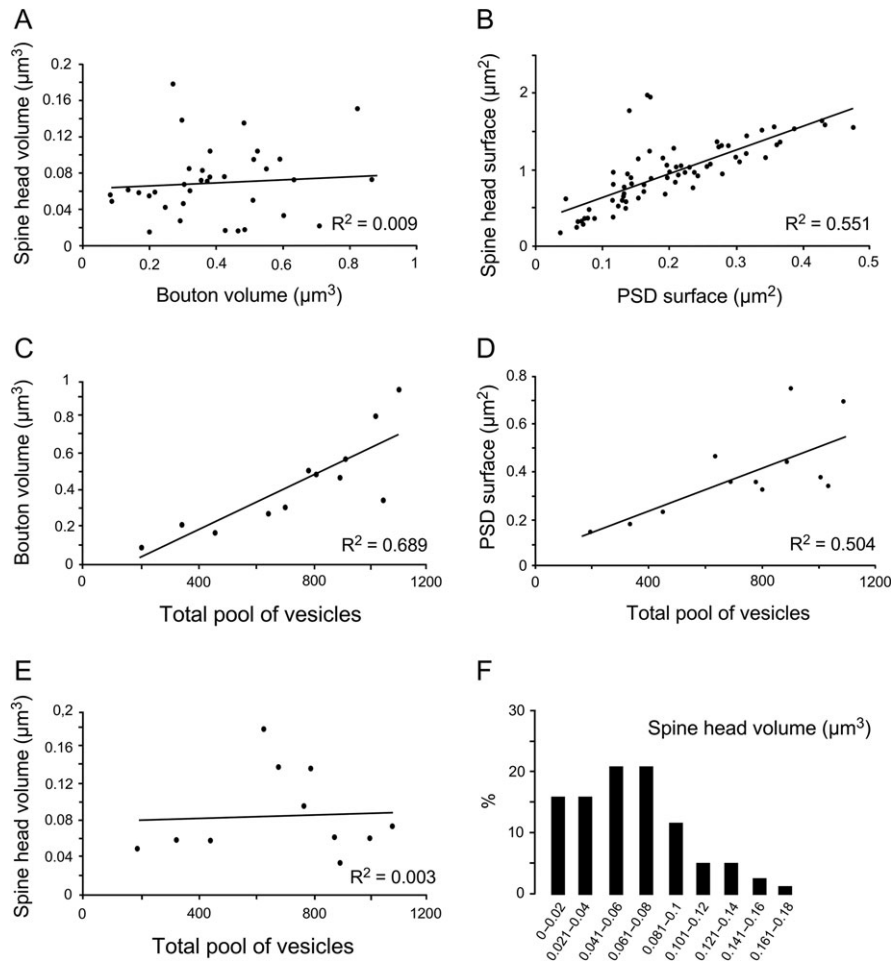
Figure 11. Correlation of structural parameters of VPMdm boutons (II). Panels A–B and F show Serial TEM and FIB/SEM data pooled together. Panels C–E display only TEM data. In the charts, dots plot correlation: (A) between bouton and spine head volume. (B) between PSD surface vs. spine head surface; (C) between the total pool of synaptic vesicles vs. bouton volume; (D) between total pool of synaptic vesicles vs. PSD contour surface area; and (E) between total pool of vesicles and spine head volume. (F) Bar histogram showing the distribution of spine head volumes in spines postsynaptic to VPMdm axons (62 serial TEM and 30 FIB/SEM).

Fig. 11F). No correlation was observed between bouton volume and dendritic spine head volume ($r = 0.095$; $P = 0.37$; Fig. 11A). However, the surface area of PSDs is highly correlated with dendritic spine head surface ($r = 0.743$; $P < 0.00001$; Fig. 11B; see also Table 1). This seems to indicate a direct relationship between the size of the dendritic spine head with that of PSDs, but not with that of the presynaptic terminal.

The total synaptic vesicle pool size was 740 ± 285 vesicles (range 200–1095 vesicles). Pool size was correlated with the volume of the synaptic bouton ($r = 0.83$; $P = 0.00033$; Fig. 11C) as well as between PSD surface and the total pool of vesicles per bouton ($r = 0.71$; $P = 0.01$; Fig. 11D). In the 12 fully reconstructed vesicle pools, the size of the pool did not correlate with the volume of the postsynaptic spine head (Fig. 11E).

Discussion

The present study represents a comprehensive quantitative 3D analysis of anterogradely labeled VPMdm synaptic boutons terminating in L4 of mouse S1. Our results reveal a number of particular features of both the pre- and postsynaptic elements that together may contribute to the "unique" properties of VPMdm synapses.

Relevance and Technical Limitations of Quantitative Analyses of Identified VPMdm Synaptic Boutons

Thalamocortical neurons link monosynaptically the thalamus with all the areas of the neocortex. Far from being a homogeneous cell population, however, TC neurons are increasingly recognized as a diverse group of glutamatergic projection cells with widely diverse dendritic and axonal branching architectures (Clascá et al. 2016). The TC axons diverge, converge and branch profusely in their path to the cortex. As a result, sensory cortices receive convergent projections from several thalamic nuclei or subnuclei that carry diverse types of information, and terminate in partly overlapping laminar patterns (reviewed in Castro-Alamancos and Connors 1997; Bosman et al. 2011). In rodents, axons from VPMdm which are of the "specific" or "lemniscal" type, topographically innervate L4 "barrel" domains in S1. In contrast, axons from the "paralemniscal" caudoventral portion of the VPM evenly innervate both L4 barrels and septa in S1 (Pierret et al. 2000; Haidarliu et al. 2008), while axons from a dorsomedial domain of the VPM selectively innervate L4 septa (Furuta et al. 2009). Moreover, axons from the "multi-specific" or "extralemniscal" Posterior nucleus innervate L4 septa (Lu and Lin 1993; Ohno et al. 2012), while the "non-specific" Ventromedial nucleus and the "intralaminar" Parafascicular
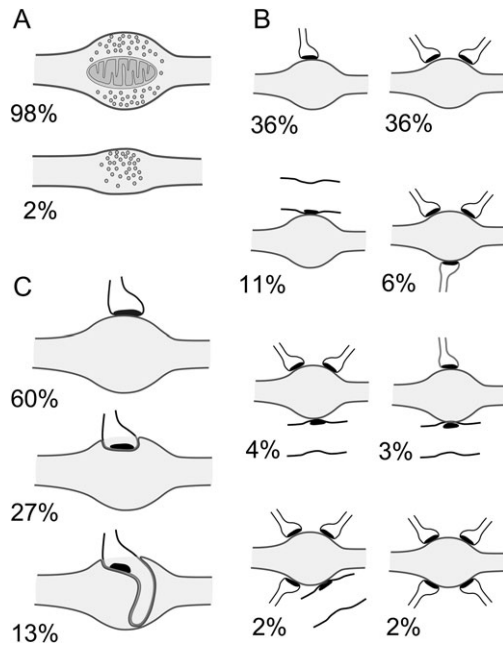
Figure 12. Graphic summary of structural features of VPMdm synaptic boutons and their innervation pattern on target structures. Serial TEM and FIB/SEM data are pooled together. (A) Synaptic boutons lacking or containing mitochondria. (B) Predominant innervation pattern of VPMdm synaptic boutons. (C) Unusual synaptic specializations observed in spines postsynaptic to VPMdm boutons. From top to bottom, a conventional apposition between a spine and a synaptic bouton covered only by the PSD at the pre-and postsynaptic apposition zone; a spine with its head partially invading the bouton, the PSD is part of the pre-and postsynaptic apposition zone; and a spine with a large and deep protrusion into the bouton. Note that the bouton perimeter remains constant whereas the spine protrusion expands inside it. See also Figure 9B,D.

nucleus (Rubio-Garrido et al. 2009; Clascá et al. 2016) contribute with additional boutons to the S1 neuropil.

Moreover, there is also growing evidence that TC synapses from different nuclei may be structurally different, in terms of presynaptic structure specializations and of the postsynaptic elements involved (Da Costa and Martin 2011; Viaene et al. 2011; Familtsev et al. 2016; Bopp et al. 2017). Keeping in mind these caveats, we took pains to produce BDA deposits limited to VPMdm (Fig. 1, Supplementary Fig. 1), and took EM samples only from L4 barrel domains (Figs 1 and 2).

However, selective labeling with anterograde tracers and subsequent quantitative 3D analysis of synaptic parameters in identified TC synaptic boutons at the fine-scale EM level has limitations. The most important is that the DAB-reaction product may interfere with the identification of subcellular elements. Our staining protocol produced a DAB precipitate that could be followed in serial ultrathin sections, but still light enough to allow the identification of most ultrastructual features (see Methods).

Several experimental approaches have been used for selectively labeling TC synapses for EM analysis, including anterograde degeneration after thalamic lesions (Jones and Powell 1970; Peters et al. 1977; White 1978; Davis and Sterling 1979) and the anterograde axonal transport of lectins (Cipolloni, et al. 1985; Keller et al. 1985; Lu and Lin 1993); biocytin (Lev et al. 2002) or BDA (White, et al. 2004; Da Costa and Martin 2009; Anderson et al. 2009; present study). BDA is particularly adequate because of its high-sensitivity and simple staining procedure, which minimizes tissue damage. Immunolabeling for vesicular glutamate transporter 2 (VGluT2) has also been used

to identify putative TC synapses (Kubota et al. 2007; 2015; Bopp et al. 2017). However, VGluT2 immunolabeling includes some non-thalamic synapses, such as those from the claustrum, and it does not allow to distinguish between the TC synapses converging from different thalamic nuclei (Hur and Zaborsky 2005; Clascá et al. 1992).

In the small mouse brain, ensuring specificity using BDA required high precision in the tracer delivery procedure (Fig. 1). Moreover, as those connections between thalamus and cortex are reciprocal, an additional concern was the possibility of retrogradely labeling BDA corticothalamic L6 neurons, which are known to extend collateral axon branches into L4 (Qi and Feldmeyer 2016). Here, we limited this possibility by using small micropipette tips, very low injection currents, and the 10 000 K moiety of BDA, which is preferentially transported in the anterograde direction (Reiner et al. 2000). As a result, labeling was massively anterograde, with only occasional, isolated cell bodies backlabeled in the cortex. In this regard, our finding that 83% of the synaptic boutons examined are located on spines is consistent with a selective labeling of TC axons, because corticothalamic L6 axon collaterals predominantly target dendritic shafts (White and Keller 1987). Likewise, the large size of boutons in our sample is also consistent with selective TC axon labeling, because rodent corticothalamic collateral branch boutons are uniformly small (White and Keller 1987; Kubota et al. 2007).

Quantitative 3D models of synaptic structures are, to date, the best solution to estimate various synaptic parameters in sufficient detail (for example for cortical synaptic boutons: Marrone et al. 2005; Rollenhagen et al. 2007, 2015; Wilke et al. 2013; Dufour et al. 2016; Bopp et al. 2017; Hsu et al. 2017; present study). However, EM 3D reconstruction of identified neuronal processes and their synapses throughout a complex neuropil require obtaining sufficiently large and continuous series of precisely aligned EM images from a precisely localized spot in the tissue (Bosch et al. 2015; Fig. 2).

We used 2 different methods to produce large series of aligned EM images, serial ultrathin sectioning + TEM analysis and FIB/SEM. Serial TEM is labor-intensive and technically demanding, and is limited to relative small regions of interest (ROIs) and z-dimensions, but, in turn, it provides the adequate resolution to sharply visualize small subcellular elements, particularly membrane compartments such as synaptic vesicles or spine apparatuses. FIB/SEM operates in semi-automatic mode and produces larger-scale ROIs with a nearly unlimited z-dimension. Moreover, the ion beam milling has been adjusted down to 25 nm which is practically impossible with conventional ultramicrotomy, and thus allows a more precise 3D rendering. However, the lower resolution that we have chosen for efficient FIB/SEM imaging limits its applicability for measuring the small subcellular structures mentioned above (Fig. 7, Supplementary Fig. 2). Although better resolutions are indeed possible, they require a smaller field of view and/or longer scanning times per frame. In this study we have chosen a compromise solution to maximize the total imaged volume (more than 2000 serial sections and over 4000 μm³), while labeled fibers and synaptic junctions are still clearly visible. On the above EM images series, we applied of state-of-the-art software tools specifically designed for 3D EM measurement (OpenCAR, Sätzler et al. 2002 and ESPINA, Morales et al. 2011).

Comparison of Structural Parameters with Previous EM Studies of TC Synaptic Boutons

For some of the subcellular elements, our findings can be readily reconciled with those of 2D EM studies of TC synaptic

boutons in mouse or rat showing that these boutons are relatively large, contain mitochondria, often establish more than 1 synaptic contact and have "complex" PSDs (Benshalom and White 1986; Lu and Lin 1993; Kharazia and Weinberg 1994; White et al. 2004). As discussed below, some of our observations are significantly different from recent 3D measurements of the more heterogeneous VGluT2 bouton population in mouse S1 L4 (Bopp et al. 2017).

Bouton Size and Synapse Numbers

The actual size (volume and surface) of synaptic boutons from an identified type of TC afferents have never been reported before. Our data indicate that VPMdm boutons are on average larger (mean 0.47 μm^3) than the average TC + claustral VGluT2 synaptic boutons in L4 of mouse S1 (mean 0.30 μm^3; Bopp et al. 2017), and even 2–5-fold larger when compared with excitatory intracortical boutons in different cortical layers of mice (mean 0.1 μm^3; Bopp et al. 2017; Hsu et al. 2017) and L4 in rats (mean 0.20 μm^3; Rollenhagen et al. 2015).

In addition, more than half of VPMdm boutons are multisynaptic (range 1–4 synapses; ratio 1.6 synapses/bouton, including those in non-varicose axonal segments; Fig. 12B). Previous studies in mouse S1 L4 reported substantially less multisynaptic boutons (25%, White et al. 2004; 20% Bopp et al. 2017). This difference may be in part due to the selective labeling of lemniscal VPMdm axons in our sample, compared to the labeling produced by larger VPM tracer injections (White et al. 2004) or VGluT2 immunolabeling (Bopp et al. 2017). In addition, a small fraction (5.3%) of synaptic contacts were located in non-varicose axonal segments (<0.5 μm diameter), in line with previous observations (~12%; White et al. 2004).

PSD Interface Area and Shape

More than half VPMdm synaptic boutons had more than 1 PSD. The synaptic interface area was relatively large (mean 0.1 μm^2), although an important variability was found (Table 1). The shape and size of the active zones, including the PSD, are strongly correlated with release probability, synaptic strength, efficacy and plasticity (Geinisman et al. 1991; Geinisman 1993; Matz et al. 2010; Holderith et al. 2012; reviewed by Südhof 2012).

In addition, ~50% of PSDs in VPMdm synaptic boutons showed complex (horseshoe, ring-like or fragmented) morphologies which is higher than reported for L4 synaptic boutons in rats (~35%), boutons in other layers of the mouse and monkey cerebral cortex (Hsu et al. 2017). Recently, it was shown that both the number of docked and reserve pool vesicles at these complex active zones significantly exceeds that of disc-like PSDs (Nava et al. 2014). In addition, a strong correlation between active zone area, complex PSDs and the number of docked and reserve pool vesicles was reported. Altogether, the comparably large size and high number of complex PSDs at VPMdm boutons suggest a high synaptic efficacy and strength.

Vesicle Pool Size

Vesicle pools in VPMdm synaptic boutons (mean 740 vesicles) are considerably larger than the pool size measured in rat L4 excitatory synapses (mean 560 vesicles; Rollenhagen et al. 2015), but smaller than in rodent hippocampal CA1 subregion (~1000; Bourne et al. 2013). Vesicle pools reported in the VGlut2 mouse L4 study (Bopp et al. 2017) were far higher (mean 1623 vesicles); however, vesicles numbers were estimated using the classic Abercrombie method in 2D and are thus not comparable.

The relatively large total pool of synaptic vesicles may suggest comparably large "readily releasable", "recycling", and "reserve" pools (Rollenhagen et al. 2015).

Role of Mitochondria

Nearly all VPMdm synaptic boutons contained mitochondria (Fig. 12A), often organized in clusters which contributed on average a quarter to the total volume, comparable to values in mouse S1 and motor cortex VGluT2-immunorreactive synaptic boutons (Bopp et al. 2017) and rat intracortical L4 synaptic boutons (Rollenhagen et al. 2015).

Mitochondria act not only as energy suppliers but also as internal Ca^{2+} stores (Pozzan et al. 2000; Rizzuto et al. 2000), and may thus regulate internal Ca^{2+} levels in nerve terminals (Perkins et al. 2010). In addition, mitochondria are highly mobile in neurons (Mironov 2006; Mironov and Symonchuk 2006) and may be involved in the mobilization of synaptic vesicles from the reserve pool (Verstreken et al. 2005; Perkins et al. 2010; Smith et al. 2016), suggesting the ability of VPMdm synapses to prevent a rapid depletion of the readily releasable and recycling pools by fast refilling from the reserve pool.

Dendritic Spines as the Main Target for VPMdm Synaptic Boutons

As already mentioned above, 83% of VPMdm synapses are on spine heads. Dendritic spine head volume and PSD surface area are correlated and consistent with previous studies in the rodents (Harris et al. 1992; Schikorski and Stevens 1999; Arellano et al. 2007; Bopp et al. 2017; Hsu et al. 2017). In addition, 15% of the postsynaptic dendritic spines receive a second, but symmetric, putatively inhibitory, contact. This proportion is similar to dendritic spines postsynaptic to the pool of VGluT2 boutons (thalamic + claustral) in layers 2–3 of rat medial frontal cortex (Kubota et al. 2007), but 2–7-fold higher than the general population of boutons making asymmetric contacts in layers 2–3 of mouse and monkey cortex (Hsu et al. 2017).

Since the dendrites of spiny stellate neurons are densely and selectively concentrated in the central regions of the L4 rodent barrel domains, it is likely that most if not all of the spines postsynaptic to our labeled boutons correspond to these neurons. The abundance of long-necked spines, which are typical of stellate cells, in our sample is also consistent with this interpretation (Da Costa 2013).

About 75% of the dendritic spines postsynaptic to VPMdm axons featured a spine apparatus. It has been shown that dendritic spines containing a spine apparatus display higher mobility, which seems to be an important feature for modulating short- and long-term plasticity (Konur and Yuste 2004; Holtmaat et al. 2005; Umeda et al. 2005).

Remarkably, 13% of all dendritic spines form a long and thick protrusion of the spine head that extends deeply into the VPMdm bouton. In these dendritic spines, the PSD is located on the spine head or at the base of the protrusion, and thus the protrusion membrane is, for its most part, non-synaptic. While the functional significance of these protrusions remains to be investigated, it is clear that they provide a large apposition surface beyond the PSD, which might be important for specific cell-to-cell interactions.

The dendritic spine protrusions observed in the present study had not been previously reported in rodents. Interestingly, comparable dendritic spine protrusions have been observed in the geniculocortical boutons in V1 L4 of the ferret (Erisir and Dreusicke 2005) and the tree shrew (Familtsev et al. 2016). These studies, however, did not 3D-reconstruct the spine protrusions to visualize

their shape or estimate their size. Since, as pointed out above, geniculocortical neurons innervarting V1 L4, like the VPMdm neurons, are archetypal "specific" or "core-type" sensory TC cells (Sherman 2012; Clascá et al. 2016), it is tempting to speculate that dendritic spine protrusions are specializations required in the powerful "specific" sensory TC synapses of rodents, carnivores and primates. Consistent with this interpretation, spine protrusions were not observed in the TC synapses of the pulvinar nucleus, a "higher-order" visual thalamic nucleus (Familtsev et al. 2016).

Conclusion

Abundant mitochondria, large vesicle pools and large PSDs most likely underlie the unusual efficacy and reliability of VPMdm bouton synapses, by allowing high release rates during repetitive stimulation. In addition, spine specializations such as large heads, spine apparatuses, and spine protrusions might contribute to the strong effect of these synapses on cortical L4 cells.

In summary, using anterograde labeling, and advanced 3D EM and software tools, we have been able to unravel VPMdm bouton structure and synaptic connections, and to measure them with precision. The data generated in this study may contribute to better understanding the "unique" function of VPMdm boutons in rodent S1 barrel cortex, and, more broadly, the impact of "lemniscal" thalamocortical pathways on cortical circuits function.

Supplementary Material

Supplementary data is available at *Cerebral Cortex* online.

Funding

Notes

References

Anderson JC, da Costa NM, Martin KA. 2009. The W cell pathway to cat primary visual cortex. J Comp Neurol. 516:20–35.

Arellano JI, Benavides-Piccione R, Defelipe J, Yuste R. 2007. Ultrastructure of dendritic spines: correlation between synaptic and spine morphologies. Front Neurosci. 1:131–143. doi:10.3389/neuro.01.1.1.010.2007.

Benshalom G, White EL. 1986. Quantification of thalamocortical synapses with spiny stellate neurons in layer IV of mouse somatosensory cortex. J Comp Neurol. 253:303–314.

Bopp R, Holler-Rickauer S, Martin KA, Schuhknecht GF. 2017. An ultrastructural study of the thalamic input to layer 4 of primary motor and primary somatosensory cortex in the mouse. J Neurosci. 37:2435–2448.

Bosch C, Martínez A, Masachs N, Teixeira CM, Fernaud I, Ulloa F, Pérez-Martínez E, Lois C, Comella JX, DeFelipe J, et al. 2015.

FIB/SEM technology and high-throughput 3D reconstruction of dendritic spines and synapses in GFP-labeled adult-generated neurons. Front Neuroanat. 9:60. doi:10.3389/fnana.2015.00060.

Bosman LW, Houweling AR, Owens CB, Tanke N, Shevchouk OT, Rahmati N, Teunissen WH, Ju C, Gong W, Koekkoek SK, et al. 2011. Anatomical pathways involved in generating and sensing rhythmic whisker movements. Front Integr Neurosci. 5:53.

Bourne JN, Chirillo MA, Harris KM. 2013. Presynaptic ultrastructural plasticity along CA3→CA1 axons during long-term potentiation in mature hippocampus. J Comp Neurol. 521: 3898–3912.

Brecht M, Sakmann B. 2002. Dynamic representation of whisker deflection by synaptic potentials in spiny stellate and pyramidal cells in the barrels and septa of layer 4 rat somatosensory cortex. J Physiol. 543:49–70.

Bruno RM, Sakmann B. 2006. Cortex is driven by weak but synchronously active thalamocortical synapses. Science. 312: 1622–1627.

Castro-Alamancos MA, Connors BW. 1997. Thalamocortical synapses. Prog Neurobiol. 51:581–606.

Cipolloni PB, Hersch SM, White EL. 1985. The use of lectin transport in the mouse central nervous system as an anterograde axonal marker for electron microscopy. Neurosci Lett. 58:43–47.

Clascá F, Avendaño C, Román-Guindo A, Llamas A, Reinoso-Suárez F. 1992. Innervation from the claustrum of the frontal association and motor areas: axonal transport studies in the cat. J Comp Neurol. 326:402–422.

Clascá F, Porrero C, Galazo MJ, Rubio-Garrido P, Evangelio M. 2016. Anatomy and development of multispecific thalamocortical axons: implications for cortical dynamic and evolution. In: Rockland KS, editor. Axons Brain Archit. Oxford: Academic Press. p. 69–92.

Colonnier M. 1968. Synaptic patterns on different cell types in the different laminae of the cat visual cortex. An electron microscope study. Brain Res. 9:268–287.

Da Costa NM. 2013. Diversity of thalamorecipient spine morphology in cat visual cortex and its implication for synaptic plasticity. J Comp Neurol. 521:2058–2066.

Da Costa NM, Martin KA. 2009. The proportion of synapses formed by the axons of the lateral geniculate nucleus in layer 4 of area 17 of the cat. J Comp Neurol. 516:264–276.

Da Costa NM, Martin KA. 2011. How thalamus connects to spiny stellate cells in the cat's visual cortex. J Neurosci. 31: 2925–2937.

Davis TL, Sterling P. 1979. Microcircuitry of cat visual cortex: classification of neurons in layer IV of area 17, and identification of the patterns of lateral geniculate input. J Comp Neurol. 188:599–628.

Dufour A, Rollenhagen A, Sätzler K, Lübke JHR. 2016. Development of synaptic boutons in layer 4 of the barrel field of the rat somatosensory cortex: a quantitative analysis. Cereb Cortex. 26:838–854.

Erisir A, Dreusicke M. 2005. Quantitative morphology and postsynaptic targets of thalamocortical axons in critical period and adult ferret visual cortex. J Comp Neurol. 485:11–31.

Familtsev D, Quiggins R, Masterson SP, Dang W, Slusarczyk AC, Petry HM, Bickford ME. 2016. Ultraestructure of geniculocortical synaptic connections in the tree shrew striate cortex. J Comp Neurol. 524:1292–1306.

Feldmeyer D, Egger V, Lübke J, Sakmann B. 1999. Reliable synaptic connections between pairs of excitatory layer 4 neurones within a single 'barrel' of developing rat somatosensory cortex. J Physiol. 521:169–190.

Ferster D, Chung S, Wheat H. 1996. Orientation selectivity of thalamic input to simple cells of cat visual cortex. Nature. 380:249–252.

Furuta T, Kaneko T, Deschênes M. 2009. Septal neurons in barrel cortex derive their receptive field input from the lemniscal pathway. J Neurosci. 29:4089–4095.

Geinisman Y. 1993. Perforated axospinous synapses with multiple, completely partitioned transmission zones: probable structural intermediates in synaptic plasticity. Hippocampus. 3:417–433.

Geinisman Y, deToledo-Morrell L, Morrell F. 1991. Induction of long-term potentiation is associated with an increase in the number of axospinous synapses with segmented postsynaptic densities. Brain Res. 566:77–88.

Gil Z, Connors BW, Amitai Y. 1999. Efficacy of thalamocortical and intracortical synaptic connections: quanta, innervation, and reliability. Neuron. 23:385–397.

Gray EG. 1959a. Electron microscopy of synaptic contacts on dendrite spines of the cerebral cortex. Nature. 183:1592–1593.

Gray EG. 1959b. Axo-somatic and axo-dendritic synapses of the cerebral cortex: an electron microscope study. J Anat. 93: 420–433.

Haidarliu S, Yu C, Robin N, Ahissar E. 2008. Lemniscal and extralemniscal compartments in the VPM of the rat. Front Neuroanat. 2:4.

Harris KM, Jensen FE, Tsao B. 1992. Three-dimensional structure of dendritic spines and synapses in rat hippocampus (CA1) at postnatal day 15 and adult ages: implications for the maturation of synaptic physiology and long-term potentiation. J Neurosci. 12:2685–2705.

Holderith N, Lorincz A, Katona G, Rózsa B, Kulik A, Watanabe M, Nusser Z. 2012. Release probability of hippocampal glutamatergic terminals scales with the size of the active zone. Nat Neurosci. 15:988–997.

Holtmaat A, Svoboda K. 2009. Experience-dependent structural synaptic plasticity in the mammalian brain. Nat Rev Neurosci. 10:647–658.

Holtmaat AJ, Trachtenberg JT, Wilbrecht L, Shepherd GM, Zhang X, Knott GW, Svoboda K. 2005. Transient and persistent dendritic spines in the neocortex in vivo. Neuron. 45: 279–291.

Hsu A, Luebke JI, Medalla M. 2017. Comparative ultrastructural features of excitatory synapses in the visual and frontal cortices of the adult mouse and monkey. J Comp Neurol. doi:10. 1002/cne.24196.

Hur EE, Zaborsky L. 2005. Vglut2 afferents to the medial prefrontal and primary somatosensory cortices: a combined retrograde tracing in situ hybridization study. J Comp Neurol. 483:351–373.

Jones EG. 1998. Viewpoint: the core and matrix of thalamic organization. Neuroscience. 85:331–345.

Jones EG, Powell TPS. 1970. An electron microscopic study of the laminar pattern and mode of termination of afferent fibre pathways in the somatic sensory cortex of the cat. Philos Trans R Soc Lond B Biol Sci. 257:45–62.

Keller A, White EL, Cipolloni PB. 1985. The identification of thalamocortical axon terminals in barrels of mouse SmI cortex using immunohistochemistry of anterogradely transported lectin (Phaseolus vulgaris-leucoagglutinin). Brain Res. 343:159–165.

Kharazia VN, Weinberg RJ. 1994. Glutamate in thalamic fibers terminating in layer IV of primary sensory cortex. J Neurosci. 14:6021–6032.

Killackey HP. 1973. Anatomical evidence for cortical subdivisions based on vertically discrete thalamic projections from

the ventral posterior nucleus to cortical barrels in the rat. Brain Res. 51:326–331.

Konur S, Yuste R. 2004. Imaging the motility of dendritic protrusions and axon terminals: roles in axon sampling and synaptic competition. Mol Cell Neurosci. 27:427–440.

Kubota Y, Hatada S, Kondo S, Karube F, Kawaguchi Y. 2007. Neocortical inhibitory terminals innervate dendritic spines targeted by thalamocortical afferents. J Neurosci. 27: 1139–1150.

Kubota Y, Kondo S, Nomura M, Hatada S, Yamaguchi N, Mohamed AA, Karube F, Lübke J, Kawaguchi Y. 2015. Functional effects of distinct innervation styles of pyramidal cells by fast spiking cortical interneurons. Elife. 4. doi:10. 7554/eLife.07919.

Kuhlman SJ, O'Connor DH, Fox K, Svoboda K. 2014. Structural plasticity within the barrel cortex during initial phases of whisker-dependent learning. J Neurosci. 34:6078–6083.

Land PW, Buffer SAJr, Yaskosky JD. 1995. Barreloids in adult rat thalamus: three-dimensional architecture and relationship to somatosensory cortical barrels. J Comp Neurol. 355: 573–588.

Lev DL, Weinfeld E, White EL. 2002. Synaptic patterns of thalamocortical afferents in mouse barrels at postnatal day 11. J Comp Neurol. 442:63–77.

Lu SM, Lin RC. 1993. Thalamic afferents of the rat barrel cortex: a light- and electron-microscopic study using Phaseolus vulgaris leucoagglutinin as an anterograde tracer. Somatosens Mot Res. 10:1–16.

Marion R, Li K, Purushothaman G, Jiang Y, Casagrande VA. 2013. Morphological and neurochemical comparisons between pulvinar and V1 projections to V2. J Comp Neurol. 521:813–832.

Marrone DF, LeBoutillier JC, Petit TL. 2005. Ultrastructural correlates of vesicular docking in the rat dentate gyrus. Neurosci Lett. 378:92–97.

Matz J, Gilyan A, Kolar A, McCarvill T, Krueger SR. 2010. Rapid structural alterations of the active zone lead to sustained changes in neurotransmitter release. Proc Natl Acad Sci USA. 107:8836–8841.

Merchán-Pérez A, Rodriguez J-R, Alonso-Nanclares L, Schertel A, Defelipe J. 2009. Counting synapses using FIB/SEM microscopy: a true revolution for ultrastructural volume reconstruction. Front Neuroanat. 3:18.

Meyer HS, Wimmer VC, Oberlaender M, de Kock CP, Sakmann B, Helmstaedter M. 2010. Number and laminar distribution of neurons in a thalamocortical projection column of rat vibrissal cortex. Cereb Cortex. 20:2277–2286.

Mironov SL. 2006. Spontaneous and evoked neuronal activities regulate movements of single neuronal mitochondria. Synapse. 59:403–411.

Mironov SL, Symonchuk N. 2006. ER vesicles and mitochondria move and communicate at synapses. J Cell Sci. 119: 4926–4934.

Morales J, Alonso-Nanclares L, Rodríguez JR, DeFelipe J, Rodríguez A, Merchán-Pérez A. 2011. Espina: a tool for the automated segmentation and counting of synapses in large stacks of electron microscopy images. Front Neuroanat. 5:18.

Morales J, Rodríguez A, Rodríguez J-R, DeFelipe J, Merchán-Pérez A. 2013. Characterization and extraction of the synaptic apposition surface for synaptic geometry analysis. Front Neuroanat. 7:20.

Nava N, Chen F, Wegener G, Popoli M, Nyengaard JR. 2014. A new efficient method for synaptic vesicle quantification reveals differences between medial prefrontal cortex

perforated and nonperforated synapses. J Comp Neurol. 522: 284–297.

Oberlaender M, de Kock CP, Bruno RM, Ramirez A, Meyer HS, Dercksen VJ, Helmstaedter M, Sakmann B. 2012. Cell type-specific three-dimensional structure of thalamocortical circuits in a column of rat vibrissal cortex. Cereb Cortex. 22: 2375–2391.

Ohno S, Kuramoto E, Furuta T, Hioki H, Tanaka YR, Fujiyama F, Sonomura T, Uemura M, Sugiyama K, Kaneko T. 2012. A morphological analysis of thalamocortical axon fibers of rat posterior thalamic nuclei: a single neuron tracing study with viral vectors. Cereb Cortex. 22:2840–2857.

Paxinos G, Franklin K. 2012. The mouse brain in stereotaxic coordinates. 4th ed. Amsterdam-Boston: Academic Press.

Perkins GA, Tjong J, Brown JM, Poquiz PH, Scott RT, Kolson DR, Ellisman MH, Spirou GA. 2010. The micro-architecture of mitochondria at active zones: electron tomography reveals novel anchoring scaffolds and cristae structured for high-rate metabolism. J Neurosci. 30:1015–1026.

Peters A, Palay SL. 1996. The morphology of synapses. J Neurocytol. 25:687–700.

Peters A, Palay SL, Webster H. 1991. The fine structure of the nervous system. Ch. 3: Dendrites. New York: Oxford University Press. p. 70–100.

Peters A, White EL, Fairén A. 1977. Synapses between identified neuronal elements. An electron microscopic demonstration of degenerating axón terminals synapsing with Golgi impregnated neurons. Neurosci Lett. 6:171–175.

Pierret T, Lavallée P, Deschênes M. 2000. Parallel streams for the relay of vibrissal information through thalamic barreloids. J Neurosci. 20:7455–7462.

Pozzan T, Magalhaes P, Rizzuto R. 2000. The comeback of mitochondria to calcium signalling. Cell Calcium. 28:279–283.

Qi G, Feldmeyer D. 2016. Dendritic target region-specific formation of synapses between excitatory layer 4 neurons and layer 6 pyramidal cells. Cereb Cortex. 26:1569–1579.

Reiner A, Veenman CL, Medina L, Jiao Y, Del Mar N, Honig MG. 2000. Pathway tracing using biotinylated dextran amines. J Neurosci Methods. 103:23–37.

Reyes-Puerta V, Sun JJ, Kim S, Kilb W, Luhmann HJ. 2015. Laminar and columnar structure of sensory-evoked multineuronal spike sequences in adult rat barrel cortex in vivo. Cereb Cortex. 25:2001–2021.

Reynolds ES. 1963. The use of lead citrate at high pH as an electron-opaque stain in electron microscopy. J Cell Biol. 17: 208–212.

Rizzuto R, Bernardi P, Pozzan T. 2000. Mitochondria as all-round players of the calcium game. J Physiol. 529:37–47.

Rollenhagen A, Klook K, Sätzler K, Qi G, Anstötz M, Feldmeyer D, Lübke JHR. 2015. Structural determinants underlying the high efficacy of synaptic transmission and plasticity at synaptic boutons in layer 4 of the adult rat barrel cortex. Brain Struct Funct. 220:3185–3209.

Rollenhagen A, Sätzler K, Rodríguez EP, Jonas P, Froscher M, Lübke JH. 2007. Structural determinants of transmission at large hippocampal mossy fiber synapses. J Neurosci. 27: 10434–10444.

Rubio-Garrido P, Pérez-de-Manzo F, Porrero C, Galazo MJ, Clascá F. 2009. Thalmic input to distal apical dendrites in neocortical layer 1 is massive and highly convergent. Cereb Cortex. 19: 2380–2395.

Sätzler K, Söhl LF, Bollmann JH, Borst JG, Frotscher M, Sakmann B, Lübke JHR. 2002. Three-dimensional reconstruction of a calyx of Held and its postsynaptic principal neuron in the medial nucleus of the trapezoid body. J Neurosci. 22:10567–10579.

Schikorski T, Stevens CF. 1999. Quantitative fine-structural analysis of olfactory cortical synapses. Proc Natl Acad Sci USA. 96:4107–4112.

Schindelin J, Arganda-Carreras I, Frise E, Kaynig V, Longair M, Pietzsch T, Preibisch S, Rueden C, Saalfeld S, Schmid B, et al. 2012. Fiji: an open-source platform for biological-image analysis. Nat Methods. 9:676–682.

Schoonover CE, Tapia JC, Schilling VC, Wimmer V, Blazeski R, Zhang W, Mason CA, Bruno RM. 2014. Comparative strength and dendritic organization of thalamocortical and cortico-cortical synapses onto excitatory layer 4 neurons. J Neurosci. 34:6746–6758.

Shepherd GM, Harris KM. 1998. Three-dimensional structure and composition of CA3–>CA1 axons in rat hippocampal slices: implications for presynaptic connectivity and compartmentalization. J Neurosci. 18:8300–8310.

Sherman SM. 2012. Thalamocortical interactions. Curr Opin Neurobiol. 22:575–579.

Shu SY, Ju G, Fan LZ. 1988. The glucose oxidase-DAB-nickel method in peroxidase histochemistry of the nervous system. Neurosci Lett. 85:169–171.

Smith HL, Bourne JN, Cao G, Chirillo MA, Ostroff LE, Watson DJ, Harris KM. 2016. Mitochondrial support of persistent presynaptic vesicle mobilization with age-dependent synaptic growth after LTP. Elife. 5:e15275.

Südhof TC. 2012. The presynaptic active zone. Neuron. 75:11–25.

Sultan F, König T, Möck M, Their P. 2002. Quantitative organization of neurotransmitters in the deep cerebellar nuclei of the Lurcher mutant. J Comp Neurol. 452:311–323.

Umeda T, Ebihara T, Okabe S. 2005. Simultaneous observation of stably associated presynaptic varicosities and postsynaptic spines: morphological alterations of CA3-CA1 synapses in hippocampal slice cultures. Mol Cell Neurosci. 28: 264–274.

Verstreken P, Ly CV, Venken KJ, Koh TW, Zhou Y, Bellen HJ. 2005. Synaptic mitochondria are critical for mobilization of reserve pool vesicles at Drosophila neuromuscular junctions. Neuron. 47:365–378.

Viaene AN, Petrof I, Sherman SM. 2011. Properties of the thalamic projection from the posterior medial nucleus to primary and secondary somatosensory cortices in the mouse. Proc Natl Acad Sci USA. 108:18156–18161.

White EL. 1978. Identified neurons in mouse SmI cortex which are postsynaptic to thalamocortical axon terminals: A combined Golgielectron microscopic and degeneration study. J Comp Neurol. 181:627–662.

White EL, Keller A. 1987. Intrinsic circuitry involving the local axonal collaterals of corticothalamic projection cells in mouse SmI cortex. J Comp Neurol. 262:13–26.

White EL, Weinfeld E, Lev DL. 2004. Quantitative analysis of synaptic distribution along thalamocortical axons in adult mouse barrels. J Comp Neurol. 479:56–69.

Wilke SA, Antonios JK, Bushong EA, Badkoobehi A, Malek E, Hwang M, Terada M, Ellisman MH, Ghosh A. 2013. Deconstructing complexity: serial block-face electron microscopic analysis of the hippocampal mossy fiber synapse. J Neurosci. 33:507–522.